Organized Trade Cumulus Clouds Suppressed by Climate Change

Jan Kazil[1,2], Pornampai Narenpitak[3], Takanobu Yamaguchi[1,2], and Graham Feingold[2]

[1]Cooperative Institute for Research in Environmental Sciences, University of Colorado Boulder, Boulder, Colorado, 80309, USA

[2]National Oceanic and Atmospheric Administration, Chemical Sciences Laboratory, Boulder, Colorado, 80305, USA

[3]Data-driven Simulation and Systems Research Team, National Electronics and Computer Technology Center, Pathumthani, 12120, Thailand

Key Points:

- Trade cumulus mesoscale organization enhances the cloud response to climate change.
- The primary cause is down-welling long-wave radiation from increased greenhouse gas concentrations.
- The cumulus-valve mechanism does not universally stabilize trade cumulus clouds against climate change.

Corresponding author: Jan Kazil, jan.kazil@noaa.gov

Abstract

We present a first study showing that organization of trade cumulus (Tc) clouds can significantly enhance Tc response to climate change. Among four recently identified states of Tc organization, the "Flower" state has the highest and the "Sugar" state the lowest cloud fraction and cloud radiative effect. Using large-eddy simulations, we show that the organized "Flower" Tc state is strongly suppressed at the end of the 21st century, unlike the less organized "Sugar" Tc state and Tc studied previously. The primary cause of the suppression is down-welling long-wave radiation from increased greenhouse gas concentrations, which weakens the mesoscale circulation that organizes clouds into the "Flower" Tc state. The cumulus-valve mechanism, which is thought to limit Tc response to climate change, does not prevent this response. Our work unravels an unrecognized role of cloud organization in the cloud response to climate change.

Plain Language Summary

Trade cumulus clouds cover large swaths of the oceans and cool the planet. Climate models struggle to capture these clouds, leading to uncertainty in climate projections. We show that among four recently identified organized types of trade cumulus clouds, the type of organization with the highest cooling effect will be strongly suppressed at the end of the 21st century, unlike less organized trade cumulus clouds with a lower cooling effect. The strong suppression is a direct consequence of cloud organization. Down-welling long-wave radiation from rising greenhouse gases is the primary cause. The role of cloud organization and the underlying physical mechanisms we identify may contribute to improving the representation of trade cumulus clouds in climate models.

1 Introduction

Low clouds cool the Earth by reflecting sunlight back to space. The cooling effect depends on the response of clouds to the climate system, and in turn affects Earth's climate. This cloud-climate feedback determines climate sensitivity, the Earth's temperature response to rising levels of greenhouse gases (GHG). The latest generation of climate models predicts a high climate sensitivity due to strong low cloud feedbacks (Zelinka et al., 2020). Observations, however, indicate a moderate climate sensitivity due to low clouds (Cesana & Del Genio, 2021; Myers et al., 2021). The discrepancy is caused in part by trade cumulus (Tc) clouds, a key source of uncertainty in climate projections (Bony & Dufresne, 2005; Vial et al., 2013; Medeiros et al., 2015). Tc feedbacks in climate models are governed by changes in cloud fraction near cloud base (Brient et al., 2016; Vial et al., 2016). Climate models with a high climate sensitivity suggest a strong decrease in Tc cloud base cloudiness owing to increased lower-tropospheric mixing and cloud base evaporation (Sherwood et al., 2014; Brient et al., 2016; Vial et al., 2016). Vogel et al. (2022) refuted this mixing-desiccation hypothesis observationally, and found that a weak Tc feedback is more plausible than a strong one, providing an important line of evidence against high climate sensitivity. Observations (Nuijens et al., 2015) and large-eddy simulations (Rieck et al., 2012; Blossey et al., 2013; Vogel et al., 2016; Tan et al., 2017) suggest that Tc are remarkably stable against climate change, and exhibit a weak positive feedback (Vial et al., 2017). The leading hypothesis for a broad stability of Tc against climate change is the cumulus-valve mechanism (Neggers et al., 2006). This hypothesis postulates a negative feedback between the cloud base cloud fraction and the mixed layer height via the cloud mass flux.

Four new manifestations of Tc organization called Sugar, Gravel, Fish, and Flowers have been identified by Stevens et al. (2020). These cloud states cool the Earth to different extents: the Sugar Tc state has the lowest and the Flower Tc state the highest cloud fraction and cloud radiative effect (Bony et al., 2020). This diversity suggests an uncharted landscape of Tc responses to climate change involving potentially unrecognized mechanisms. We explore the role of organization of the Flower and Sugar Tc states to anthropogenic climate change from present-day (PD) to end-of-21st-century (EC) conditions. 21st century climate change is represented using the RCP8.5 scenario, which is the best match out to midcentury under current and stated policies, with still highly plausible levels of CO_2 emissions in 2100 (Schwalm et al., 2020). CO_2 approximately dou-

bles, and in the region considered here, sea surface temperature (SST) increases by 1.8 K from PD to EC. We divide climate change into effects from SST and large scale meteorology (LSM), and effects from GHG down-welling long-wave (LW) radiation. LSM consists of atmospheric temperature, water vapor, zonal and meridional wind speed, and subsidence.

We use Lagrangian large eddy simulations (Kazil et al., 2021; Narenpitak et al., 2021) that track Tc evolution along two trajectories east of Barbados (Fig. SF1). Along a northern trajectory, three simulations ($\mathcal{F}_{\mathrm{PD}}$, $\mathcal{F}^{-}_{\mathrm{EC}}$, $\mathcal{F}_{\mathrm{EC}}$) simulate the Flower Tc state but differ in their forcings. $\mathcal{F}_{\mathrm{PD}}$ uses $\mathrm{SST}_{\mathrm{PD}}$, $\mathrm{LSM}_{\mathrm{PD}}$, and $\mathrm{GHG}_{\mathrm{PD}}$. $\mathcal{F}^{-}_{\mathrm{EC}}$ uses $\mathrm{SST}_{\mathrm{EC}}$, $\mathrm{LSM}_{\mathrm{EC}}$, but $\mathrm{GHG}_{\mathrm{PD}}$. $\mathcal{F}_{\mathrm{EC}}$ uses $\mathrm{SST}_{\mathrm{EC}}$, $\mathrm{LSM}_{\mathrm{EC}}$, and $\mathrm{GHG}_{\mathrm{EC}}$. Simulations of the Sugar Tc state ($\mathcal{S}_{\mathrm{PD}}$, $\mathcal{S}_{\mathrm{EC}}$) are constructed from the Flower simulations along the northern trajectory by holding the subsidence profile constant starting from 8 h into the simulations (Fig. SF5). This suppresses large scale upward motion and keeps the cloud field in the Sugar Tc state until sunset. The role of large scale vertical motion for the evolution of the Flower Tc state is discussed by Narenpitak et al. (2021). The simulation $\mathcal{S}_{\mathrm{PD}}$ uses $\mathrm{SST}_{\mathrm{PD}}$, $\mathrm{LSM}_{\mathrm{PD}}$, and $\mathrm{GHG}_{\mathrm{PD}}$, simulation $\mathcal{S}_{\mathrm{EC}}$ uses $\mathrm{SST}_{\mathrm{EC}}$, $\mathrm{LSM}_{\mathrm{EC}}$, and $\mathrm{GHG}_{\mathrm{EC}}$. We quantify the response of the Flower Tc state to the change from PD to EC in SST and LSM, and down-welling LW from GHG. We identify the underlying physical mechanisms, and compare the response of the Flower Tc state to that of the Sugar Tc state and to Tc studied previously. Along a southern trajectory, the simulations $\mathcal{F}^{*}_{\mathrm{PD}}$, $\mathcal{F}^{*}_{\mathrm{EC}}$ explore the response to the change from PD to EC of the Flower Tc state in different conditions, and the simulations $\mathcal{F}^{**}_{\mathrm{PD}}$, and $\mathcal{F}^{**}_{\mathrm{EC}}$ test the sensitivity of the results to resolution.

We use the System for Atmospheric Modeling (SAM, Khairoutdinov & Randall, 2003). The SST, LSM, and GHG forcing of our simulations is constructed from the ERA5 reanalysis (Hersbach et al., 2020) along the simulation trajectories, and from CMIP5 (Taylor et al., 2012) simulations under the RCP8.5 scenario with CESM1(WACCM) (Marsh et al., 2013). The model, trajectories, PD and EC forcings, and simulations are described in the *Supporting Information* (SI).

2 Results

2.1 Flowers

Figure 1 displays the simulated Tc evolution. The cloud field at sunrise (09h47m UTC) is in the Sugar Tc state across the simulations, without discernible organization. In the Flower simulations $\mathcal{F}_{\mathrm{PD}}$, $\mathcal{F}_{\mathrm{EC}}^{-}$, and $\mathcal{F}_{\mathrm{EC}}$ the cumulus clouds first cluster and then aggregate into Flowers as the day progresses, with characteristic stratiform patches from cloud top outflows (Stevens et al., 2020; Bony et al., 2020; Narenpitak et al., 2021; Schulz et al., 2021). The Flowers produce surface precipitation and a first generation of cold pools by sunset (21h18m UTC). The effect of SST increase and LSM change ($\mathcal{F}_{\mathrm{PD}}$ to $\mathcal{F}_{\mathrm{EC}}^{-}$) and of increased GHG levels ($\mathcal{F}_{\mathrm{EC}}^{-}$ to $\mathcal{F}_{\mathrm{EC}}$) imprints itself by weakening cumulus clustering, aggregation, and Flower formation, and reduces the number and size of cold pools (Fig. 1a-c). The effect is subdued from $\mathcal{F}_{\mathrm{PD}}$ to $\mathcal{F}_{\mathrm{EC}}^{-}$ and conspicuous from $\mathcal{F}_{\mathrm{EC}}^{-}$ to $\mathcal{F}_{\mathrm{EC}}$: $\mathcal{F}_{\mathrm{EC}}$ exhibits a much reduced number and size of Flowers and cold pools.

Figure 2a-c shows the time series of cloud fraction (CF), liquid water path (LWP), and short-wave cloud radiative effect (SWCRE) in the simulations. In the Flower simulations, as the Flower state evolves, the response of CF, LWP, and SWCRE to climate warming strengthens. Table 1 gives the change in CF, LWP, and SWCRE between the simulations, mean values for each simulation are given in Table ST1. Warming due to the changes in SST and LSM ($\mathcal{F}_{\mathrm{PD}}$ to $\mathcal{F}_{\mathrm{EC}}^{-}$) drives less of a response than the increase in GHG ($\mathcal{F}_{\mathrm{EC}}^{-}$ to $\mathcal{F}_{\mathrm{EC}}$): CF and LWP fall by a smaller amount from $\mathcal{F}_{\mathrm{PD}}$ to $\mathcal{F}_{\mathrm{EC}}^{-}$, and by a larger amount from $\mathcal{F}_{\mathrm{EC}}^{-}$ to $\mathcal{F}_{\mathrm{EC}}$. Consequently, SWCRE is less sensitive to change in SST and LSM, and more sensitive to increased GHG: SWCRE weakens from $\mathcal{F}_{\mathrm{PD}}$ to $\mathcal{F}_{\mathrm{EC}}^{-}$ by $0.5\,\mathrm{Wm}^{-2}$ and from $\mathcal{F}_{\mathrm{EC}}^{-}$ to $\mathcal{F}_{\mathrm{EC}}$ by $0.7\,\mathrm{Wm}^{-2}$.

We now identify the mechanisms by which climate warming suppresses the Flower Tc state. Figure 3 shows the change in mean profiles from $\mathcal{F}_{\mathrm{PD}}$ to $\mathcal{F}_{\mathrm{EC}}^{-}$ (Fig. 3a-d) and from $\mathcal{F}_{\mathrm{EC}}^{-}$ to $\mathcal{F}_{\mathrm{EC}}$ (Fig. 3e-h). We focus on the period until sunset, around which intermittent precipitation (Fig. SF9i, SF10) contributes a stochastic component whose elimination would require averaging over ensembles. From $\mathcal{F}_{\mathrm{PD}}$ to $\mathcal{F}_{\mathrm{EC}}^{-}$, which differ in SST and LSM, warmer air takes up more moisture from the ocean. This causes a stronger vertical moisture flux in the sub-cloud layer and across cloud base, but not up to the inversion (Fig. 3a). This pattern shapes the response of liquid water; it is enhanced at cloud base and in the lower part of the cloud layer, but reduced around the inversion (Fig. 3b).

Why does boundary layer circulation not carry the enhanced moisture flux all the way to the inversion in $\mathcal{F}_{\mathrm{EC}}^{-}$? The cause is the lapse rate reduction from PD to EC (Fig. SF4f), which results in greater atmospheric stability above the mixed layer in the simulations (Fig. SF7). To maintain intensity of circulation in the more stable EC conditions, turbulence kinetic energy (TKE) production would need to increase. TKE production does increase from $\mathcal{F}_{\mathrm{PD}}$ to $\mathcal{F}_{\mathrm{EC}}^{-}$ in the lower part of the cloud layer (Fig. 3c) due to enhanced latent heat release from higher vertical moisture transport (Fig. 3a). In the upper part of the cloud layer and around the inversion, however, TKE production decreases from $\mathcal{F}_{\mathrm{PD}}$ to $\mathcal{F}_{\mathrm{EC}}^{-}$. This decrease is caused by stronger radiative heating around the inversion (Fig. 3d). Decomposition of the radiative heating rate change into short-wave (SW) and LW components shows that it is stronger LW heating that is responsible for the overall stronger heating around the inversion (Fig. SF14). At the inversion, down-welling LW increases more than up-welling LW from $\mathcal{F}_{\mathrm{PD}}$ to $\mathcal{F}_{\mathrm{EC}}^{-}$, by approximately $2\,\mathrm{Wm}^{-2}$ (Fig. SF15). The increase in radiative heating around the inversion is hence primarily caused by down-welling LW from the warmer atmosphere above, which is also a consequence of the lapse rate reduction from PD to EC. The stronger heating causes an enhanced temperature increase around the inversion from $\mathcal{F}_{\mathrm{PD}}$ to $\mathcal{F}_{\mathrm{EC}}^{-}$ (Fig. SF14d), which stabilizes the air and suppresses TKE production.

From $\mathcal{F}_{\mathrm{EC}}^{-}$ to $\mathcal{F}_{\mathrm{EC}}$, which differ in GHG levels, the vertical moisture flux and liquid water content decrease, most strongly around the inversion (Fig. 3e, f). TKE production is reduced as well, primarily below the inversion and in the upper part of the cloud layer (Fig. 3g). Here too, the cause is an increase in radiative heating at and around the inversion (Fig. 3h). Decomposition of the radiative heating rate into SW and LW components shows that it is stronger LW heating that is responsible for the overall stronger heating around the inversion (Fig. SF16). Down-welling LW increases more than up-welling LW from $\mathcal{F}_{\mathrm{EC}}^{-}$ to $\mathcal{F}_{\mathrm{EC}}$ at the inversion, by approximately $7\,\mathrm{Wm}^{-2}$ (Fig. SF17). The increase in radiative heating around the inversion is hence caused by down-welling LW from increased GHG levels. The stronger heating causes an enhanced temperature increase around the inversion from $\mathcal{F}_{\mathrm{EC}}^{-}$ to $\mathcal{F}_{\mathrm{EC}}$ (Fig. SF16d), which stabilizes the air and suppresses TKE production.

Both from $\mathcal{F}_{\mathrm{PD}}$ to $\mathcal{F}_{\mathrm{EC}}^{-}$ and from $\mathcal{F}_{\mathrm{EC}}^{-}$ to $\mathcal{F}_{\mathrm{EC}}$, the Flower Tc state is suppressed. From $\mathcal{F}_{\mathrm{PD}}$ to $\mathcal{F}_{\mathrm{EC}}^{-}$, which captures the effect of end-of-century SST and LSM, offsetting mechanisms are at play: the warmer atmosphere takes up more moisture from the ocean,

which results in a stronger moisture supply to the cloud layer, and a stronger TKE production in its lower portion, both mechanisms that strengthen cloudiness. Concurrently, a reduced lapse rate opposes moisture transport to the inversion and strengthens down-welling LW radiation from the free troposphere, which warms the air around the inversion and suppresses TKE production. In combination, these mechanisms weakly suppress the Flower Tc state. In contrast, from $\mathcal{F}_{\mathrm{EC}}^{-}$ to $\mathcal{F}_{\mathrm{EC}}$, which captures the effect of increased GHG levels via LW radiation, there are no such offsetting mechanisms, and the increase in down-welling LW at the inversion is stronger compared to the step $\mathcal{F}_{\mathrm{PD}}$ to $\mathcal{F}_{\mathrm{EC}}^{-}$. The result is a strong suppression of the Flower Tc state.

2.2 Sugar

In the simulations $\mathcal{S}_{\mathrm{PD}}$ and $\mathcal{S}_{\mathrm{EC}}$, the Sugar Tc state persists throughout the day, with some clustering (Fig. 1d, e). Flowers begin to form only at sunset. The response to climate change of the Sugar Tc state ($\mathcal{S}_{\mathrm{PD}}$ to $\mathcal{S}_{\mathrm{EC}}$) differs from the response of the Flower Tc state ($\mathcal{F}_{\mathrm{PD}}$ to $\mathcal{F}_{\mathrm{EC}}$). During daytime, CF, LWP, and SWCRE change only imperceptibly from $\mathcal{S}_{\mathrm{PD}}$ to $\mathcal{S}_{\mathrm{EC}}$ compared to the change from $\mathcal{F}_{\mathrm{PD}}$ to $\mathcal{F}_{\mathrm{EC}}$ (Fig. 2a-c). The response becomes more discernible around sunset, when Flowers emerge in $\mathcal{S}_{\mathrm{PD}}$ and $\mathcal{S}_{\mathrm{EC}}$ (Fig. 1d, e, 21h18m UTC). We quantify the sensitivity of the two cloud states with the relative change of CF, LWP, and SWCRE from PD to EC, expressed per K of SST change. This reveals that the Flower Tc state is twice as sensitive as the Sugar Tc state to climate warming (Tab. 1). The Flower Tc state is also approximately twice as sensitive to climate warming in terms of SWCRE compared to the cumulus clouds studied by Blossey et al. (2013), which was found to be insensitive to GHG levels, and hence to down-welling LW radiation (Bretherton et al., 2013).

2.3 The Role of Organization

Fig. 2d-f shows spectra of TKE production, water vapor, and SWCRE at 18h00m UTC, when Flowers are present $\mathcal{F}_{\mathrm{PD}}$, $\mathcal{F}_{\mathrm{EC}}^{-}$, and $\mathcal{F}_{\mathrm{EC}}$, but not in $\mathcal{S}_{\mathrm{PD}}$ and $\mathcal{S}_{\mathrm{EC}}$ (Fig. 1). In the Flower simulations, the spectra have a strong mesoscale peak at 48 km. The TKE production peak (Fig. 2d) drives circulation that aggregates moisture (Fig. 2e), creating mesoscale moist patches (Bretherton & Blossey, 2017) where Flower clouds form (Narenpitak et al., 2021). The result is a prominent SWCRE mesoscale peak (Fig. 2f). In contrast to the Flower Tc state, the Sugar Tc state exhibits smaller mesoscale peaks. These reflect

clustering of individual cumulus clouds in the Sugar Tc state (Fig. 1d, e). The mesoscale peaks in the spectra experience a stronger response from PD to EC in the Flower Tc state compared to the Sugar Tc state (Fig. 2d-f). In particular, the spectral response of SWCRE from PD to EC is much stronger in the Flower Tc state compared to the Sugar Tc state, and confined to the mesoscale (Fig. 2f). Hence the suppression of the Flower Tc state by climate warming, by the mechanisms identified above, arises from selective weakening of mesoscale circulation that generates the Flower Tc state.

2.4 Cumulus-Valve Mechanism

The higher sensitivity to climate warming of the Flower Tc state compared to the Sugar Tc state appears in the vertical profiles of cloud mass flux and CF (Fig. SF13). From PD to EC, the cloud mass flux, and in particular CF, display a stronger decrease in the cloud top region of the Flower Tc state compared to the Sugar Tc state. The decrease in CF near cloud top of the Flower Tc state reflects a reduction of the stratiform cloud patches that form from cloud top outflows. At cloud base, cloud mass flux and CF remain unchanged from PD to EC (Fig. SF9d, e; SF11d, e) prior to onset of drizzle and precipitation (Fig. SF9h, i; SF11h, i). This stability is consistent with the cumulus-valve hypothesis. Yet, this does not prevent the response of the Flower Tc state, which arises from the suppression of mesoscale circulation in the cloud layer.

2.5 Sensitivity Tests

To test the response of the Flower Tc state in different conditions, $\mathcal{F}^*_{\mathrm{PD}}$ and $\mathcal{F}^*_{\mathrm{EC}}$ simulate the Flower Tc state along the southern trajectory (Fig. SF1). The southern trajectory has a warmer SST, a lower estimated inversion strength, and an initally faster wind speed (Fig. SF2), all of which favor cloud development. Visual inspection reveals that Flower clouds form earlier in $\mathcal{F}^*_{\mathrm{PD}}$ and $\mathcal{F}^*_{\mathrm{EC}}$ (Fig. SF18a, b) compared to $\mathcal{F}_{\mathrm{PD}}$ and $\mathcal{F}_{\mathrm{EC}}$ (Fig. 1a, b). Daytime CF and LWP are elevated in $\mathcal{F}^*_{\mathrm{PD}}$ and $\mathcal{F}^*_{\mathrm{EC}}$ (Fig. SF19a, b) compared to $\mathcal{F}_{\mathrm{PD}}$ and $\mathcal{F}_{\mathrm{EC}}$ (Fig. 2a, b). Moving from PD to EC conditions ($\mathcal{F}^*_{\mathrm{PD}}$ to $\mathcal{F}^*_{\mathrm{EC}}$), Flower formation is delayed (Fig. SF18a, b). CF, LWP, and SWCRE are more strongly reduced from $\mathcal{F}^*_{\mathrm{PD}}$ to $\mathcal{F}^*_{\mathrm{EC}}$ compared to from $\mathcal{F}_{\mathrm{PD}}$ to $\mathcal{F}_{\mathrm{EC}}$ (Tab. 1). The stronger suppression of SWCRE from $\mathcal{F}^*_{\mathrm{PD}}$ to $\mathcal{F}^*_{\mathrm{EC}}$ arises from the overall stronger reduction in CF and LWP, but also because CF and LWP peak closer to noon in $\mathcal{F}^*_{\mathrm{PD}}$, and later in $\mathcal{F}^*_{\mathrm{EC}}$ (Fig. SF19a, b). This delay exposes the CF and LWP peaks in $\mathcal{F}^*_{\mathrm{PD}}$ to stronger and in

$\mathcal{F}^{*}_{\mathrm{EC}}$ to weaker insolation, which adds to a reduced SWCRE (Fig. SF19c). The simulations along the southern trajectory, with a stronger suppression of the Flower Tc state compared to the northern trajectory from PD to EC conditions, suggest that the suppression of the Flower Tc state by climate change is a systematic phenomenon.

Our analysis has found that the sensitivity of CF of the Flower Tc state from PD to EC conditions is confined to the cloud top region. This raises the question whether the finite vertical resolution in the simulations may cause spurious mixing and cloud evaporation that renders the top region and the stratiform patches of Flower clouds overly sensitive to the change in conditions from PD to EC. Simulation $\mathcal{F}^{**}_{\mathrm{PD}}$ and $\mathcal{F}^{**}_{\mathrm{EC}}$ use a vertical grid spacing that is refined relative to $\mathcal{F}^{*}_{\mathrm{PD}}$ and $\mathcal{F}^{*}_{\mathrm{EC}}$ from 50 to 25 m across the cloud layer (Tab. ST3). In PD conditions, $\mathcal{F}^{**}_{\mathrm{PD}}$ produces visibly larger and denser stratiform Flower cloud patches (Fig. SF18c) compared to $\mathcal{F}^{*}_{\mathrm{PD}}$ (Fig. SF18a). In EC conditions, in $\mathcal{F}^{**}_{\mathrm{EC}}$ relative to $\mathcal{F}^{*}_{\mathrm{EC}}$, the effect is more subtle (Fig. SF18d and SF18b). Averaged over the simulations, the vertical grid refinement strengthens CF, LWP, and SWCRE more in PD conditions compared to EC conditions (Tab. ST1), resulting in their stronger reduction from PD to EC (Tab. 1). Spurious effects from a finite vertical resolution hence lead to a stronger underestimation of cloud top cloudiness of the Flower Tc state when it is more widespread, in PD conditions. This implies that the simulations underestimate the response of the Flower Tc state from PD to EC conditions.

3 Discussion and Conclusions

We present a first study of the response to climate change of two recently identified manifestations of Tc organization, the organized Flower Tc state and the less organized Sugar Tc state (Stevens et al., 2020; Bony et al., 2020). Using Lagrangian large eddy simulations forced by reanalysis meteorology and change in large scale conditions from climate simulations over the 21st century, we demonstrate that organization enhances the response of the Flower Tc state to climate change. Anthropogenic climate warming at the end of the 21st century strongly suppresses the organized Flower Tc state, resulting in smaller Flower-type clouds. The response is primarily caused by stronger down-welling LW radiation from increased GHG levels, and secondarily by the change in SST and LSM over the course of the 21st century. The stronger down-welling LW radiation warms and stabilizes air near the trade inversion and weakens the mesoscale circulation which organizes clouds into the Flower Tc state. This renders the Flower Tc state twice

as sensitive in terms of SWCRE response to climate warming compared to the Sugar Tc state, and compared to Tc studied previously (Blossey et al., 2013). Stability against climate warming of Tc identified in previous research is thought to be caused by the cumulus-valve mechanism (Neggers et al., 2006). Both the Flower and Sugar Tc state in our simulations exhibit a stable cloud base cloud fraction and mass flux, consistent with the cumulus-valve mechanism. However, we find that this does not prevent the strong response of the Flower Tc state to climate warming, because the response arises from mesoscale circulation in the cloud layer. Hence the cumulus-valve mechanism does not stabilize all Tc against climate change.

Our simulations cover a limited range of conditions and Flower Tc state evolutions. More comprehensive studies are needed to assess the prevalence of the phenomenon and to quantify its role for cloud feedbacks on a global scale. Such studies could reveal a role of mesoscale circulation and organization for cloud-climate feedbacks in the Gravel and Fish Tc states, and in the Tc aggregates that resulted in the discovery of mesoscale moisture aggregation as an organizing mechanism of Tc clouds (Bretherton & Blossey, 2017). A diverse response of Tc to climate change and a role of cloud state organization would present a more complex challenge in representing Tc feedbacks in climate simulations. Climate models do not differentiate between individual Tc states, and therefore do not capture cloud feedback associated with the expected change in their occurrence as the Earth warms (Bony et al., 2020; Schulz et al., 2021). Climate models also do not resolve the response and feedback of the individual Tc states to climate change, including a response of mesoscale circulation to stronger down-welling LW radiation at future GHG levels. The issue is compounded because observational studies (Denby, 2020; Scott et al., 2020; Cesana & Del Genio, 2021; Myers et al., 2021; Schulz et al., 2021) do not detect the effect of down-welling LW from increasing GHG on clouds and their spatial organization, and do not constrain the associated cloud-climate feedbacks.

This highlights the need for better understanding of cloud organization for Tc feedbacks and improved approaches for Tc representation in climate models, in order to reduce uncertainty of climate projections. High resolution simulations and large-eddy simulations (LES) can provide the physical understanding of the various Tc states and their behavior in response to climate change, and help formulate improved representations of Tc in climate models that account for cloud organization. Still, constraints of Tc feebacks from simulations, which need to connect large scale dynamics, mesoscale organ-

ization, boundary layer dynamics, and cloud processes, may remain encumbered by limited resolution, as in the case of climate models, or limited spatial and temporal extent, as in the case of high resolution simulations and LES. The promise of an independent approach to constrain Tc feedbacks might be found in the application of machine learning methods trained on observational data and reanalysis products (Denby, 2020) to climate simulations to identify individual cloud states, in combination with an emulator-based quantification of the cloud radiative effect based on LES (Feingold et al., 2016). Thus, more than one approach to constraining the Tc feedback to climate is emerging on the horizon, not only as an opportunity to improve understanding and quantification of cloud-climate interactions, but also as checks and balances on one another.

Open Research Section

The System for Atmospheric Modeling (SAM, Khairoutdinov & Randall, 2003) is available from `http://rossby.msrc.sunysb.edu/~marat/SAM.html`. The fifth generation of the European Centre for Medium-Range Weather Forecasts (ECMWF) atmospheric reanalysis (ERA5, Hersbach et al., 2020) is available through the Copernicus Climate Change Service (`https://doi.org/10.24381/cds.bd0915c6`). CESM1(WACCM) model output for the RCP8.5 scenario (National Science Foundation; US Department of Energy; National Center for Atmospheric Research, 2017) is available from `https://catalogue.ceda.ac.uk/uuid/beb9587bd78f4e959869d5c9dbd8a4ce`. The Hybrid Single Particle Lagrangian Integrated Trajectory Model (HYSPLIT, Stein et al., 2015) is available from `https://www.arl.noaa.gov/hysplit`. Simulation forcings and results are available at `https://csl.noaa.gov/groups/csl9/datasets/data/cloud_phys/2023a-Kazil-et-al`.

Acknowledgments

This study was supported by NOAA's Climate Program Office, Climate Variability and Predictability Program (GC19-303). The authors thank Marat Khairoutdinov, Stony Brook University, for providing the System for Atmospheric Modeling (SAM). The authors acknowledge the NOAA Research and Development High Performance Computing Program for providing computing and storage resources.

References

Blossey, P. N., Bretherton, C. S., Zhang, M., Cheng, A., Endo, S., Heus, T., ... Xu, K.-M. (2013). Marine low cloud sensitivity to an idealized climate change: The CGILS LES intercomparison. *J. Adv. Model. Earth Syst.*, *5*, 234–258. doi: 10.1002/jame.20025

Bony, S., & Dufresne, J.-L. (2005). Marine boundary layer clouds at the heart of tropical cloud feedback uncertainties in climate models. *Geophys. Res. Lett.*, *32*, 20806. doi: 10.1029/2005GL023851

Bony, S., Schulz, H., Vial, J., & Stevens, B. (2020). Sugar, gravel, fish, and flowers: Dependence of mesoscale patterns of trade-wind clouds on environmental conditions. *Geophys. Res. Lett.*, *47*(7), e2019GL085988. doi: 10.1029/2019GL085988

Bretherton, C. S., & Blossey, P. N. (2017). Understanding mesoscale aggregation of shallow cumulus convection using large-eddy simulation. *J. Adv. Model. Earth Syst.*, *9*(8), 2798–2821. doi: 10.1002/2017MS000981

Bretherton, C. S., Blossey, P. N., & Jones, C. R. (2013). Mechanisms of marine low cloud sensitivity to idealized climate perturbations: A single-LES exploration extending the CGILS cases. *J. Adv. Model. Earth Syst.*, *5*, 316–337. doi: 10.1002/jame.20019

Brient, F., Schneider, T., Tan, Z., Bony, S., Qu, X., & Hall, A. (2016). Shallowness of tropical low clouds as a predictor of climate models response to warming. *Climate Dynamics*, *47*(1), 433–449. doi: 10.1007/s00382-015-2846-0

Cesana, G. V., & Del Genio, A. D. (2021). Observational constraint on cloud feedbacks suggests moderate climate sensitivity. *Nature Climate Change*, *11*(3), 213–218. doi: 10.1038/s41558-020-00970-y

Denby, L. (2020). Discovering the Importance of Mesoscale Cloud Organization Through Unsupervised Classification. *Geophys. Res. Lett.*, *47*(1), e2019GL085190. doi: https://doi.org/10.1029/2019GL085190

Feingold, G., McComiskey, A., Yamaguchi, T., Johnson, J. S., Carslaw, K. S., & Schmidt, K. S. (2016). New approaches to quantifying aerosol influence on the cloud radiative effect. *Proc. Nat. Acad. Sci.*, *113*(21), 5812–5819. doi: 10.1073/pnas.1514035112

Hersbach, H., Bell, B., Berrisford, P., Hirahara, S., Horány, A., Muñoz Sabater, J.,

... Thépaut, J.-N. (2020). The ERA5 global reanalysis. *Quarterly Journal of the Royal Meteorological Society*, *146*(730), 1999–2049. doi: 10.1002/qj.3803

Kazil, J., Christensen, M. W., Abel, S. J., Yamaguchi, T., & Feingold, G. (2021). Realism of lagrangian large eddy simulations driven by reanalysis meteorology: Tracking a pocket of open cells under a biomass burning aerosol layer. *J. Adv. Model. Earth Syst.*, *13*(12), e2021MS002664. doi: 10.1029/2021MS002664

Khairoutdinov, M. F., & Randall, D. A. (2003). Cloud resolving modeling of the ARM summer 1997 IOP: Model formulation, results, uncertainties, and sensitivities. *J. Atmos. Sci.*, *60*(4), 607–625. doi: 10.1175/1520-0469(2003)060⟨0607:CRMOTA⟩2.0.CO;2

Marsh, D. R., Mills, M. J., Kinnison, D. E., Lamarque, J.-F., Calvo, N., & Polvani, L. M. (2013). Climate change from 1850 to 2005 simulated in CESM1(WACCM). *J. Clim.*, *26*(19), 7372–7391. doi: 10.1175/JCLI-D-12-00558.1

Medeiros, B., Stevens, B., & Bony, S. (2015). Using aquaplanets to understand the robust responses of comprehensive climate models to forcing. *Climate Dynamics*, *44*(7), 1957–1977. doi: 10.1007/s00382-014-2138-0

Myers, T. A., Scott, R. C., Zelinka, M. D., Klein, S. A., Norris, J. R., & Caldwell, P. M. (2021). Observational constraints on low cloud feedback reduce uncertainty of climate sensitivity. *Nature Climate Change*, *11*(6), 501–507. doi: 10.1038/s41558-021-01039-0

Narenpitak, P., Kazil, J., Yamaguchi, T., Quinn, P., & Feingold, G. (2021). From sugar to flowers: A transition of shallow cumulus organization during ATOMIC. *J. Adv. Model. Earth Syst.*, *13*(10), e2021MS002619. doi: 10.1029/2021MS002619

National Science Foundation; US Department of Energy; National Center for Atmospheric Research. (2017). *WCRP CMIP5: The NSF-DOE-NCAR team CESM1-WACCM model output for the rcp85 experiment.* Centre for Environmental Data Analysis.

Neggers, R., Stevens, B., & Neelin, J. (2006). A simple equilibrium model for shallow-cumulus-topped mixed layers. *Theor. Comput. Fluid Dyn.*, *20*, 305–322. doi: 10.1007/s00162-006-0030-1

Nuijens, L., Medeiros, B., Sandu, I., & Ahlgrimm, M. (2015). The behavior of

trade-wind cloudiness in observations and models: The major cloud components and their variability. *J. Adv. Model. Earth Syst.*, *7*(2), 600–616. doi: 10.1002/2014MS000390

Rieck, M., Nuijens, L., & Stevens, B. (2012). Marine boundary layer cloud feedbacks in a constant relative humidity atmosphere. *J. Atmos. Sci.*, *69*(8), 2538–2550. doi: 10.1175/JAS-D-11-0203.1

Schulz, H., Eastman, R., & Stevens, B. (2021). Characterization and evolution of organized shallow convection in the downstream north atlantic trades. *J. Geophys. Res.*, *126*(17), e2021JD034575. doi: 10.1029/2021JD034575

Schwalm, C. R., Glendon, S., & Duffy, P. B. (2020). RCP8.5 tracks cumulative CO_2 emissions. *Proc. Nat. Acad. Sci.*, *117*(33), 19656–19657. doi: 10.1073/pnas.2007117117

Scott, R. C., Myers, T. A., Norris, J. R., Zelinka, M. D., Klein, S. A., Sun, M., & Doelling, D. R. (2020). Observed sensitivity of low-cloud radiative effects to meteorological perturbations over the global oceans. *J. Clim.*, *33*(18), 7717–7734. doi: 10.1175/JCLI-D-19-1028.1

Sherwood, S., Bony, S., & Dufresne, J.-L. (2014). Spread in model climate sensitivity traced to atmospheric convective mixing. *Nature*, *505*, 37–42. doi: 10.1038/nature12829

Stein, A. F., Draxler, R. R., Rolph, G. D., Stunder, B. J. B., Cohen, M. D., & Ngan, F. (2015). NOAA's HYSPLIT Atmospheric Transport and Dispersion Modeling System. *Bulletin of the American Meteorological Society*, *96*(12), 2059–2077. doi: 10.1175/BAMS-D-14-00110.1

Stevens, B., Bony, S., Brogniez, H., Hentgen, L., Hohenegger, C., Kiemle, C., ... Zuidema, P. (2020). Sugar, gravel, fish and flowers: Mesoscale cloud patterns in the trade winds. *Q. J. R. Meteorol. Soc.*, *146*(726), 141–152. doi: 10.1002/qj.3662

Tan, Z., Schneider, T., Teixeira, J., & Pressel, K. G. (2017). Large-eddy simulation of subtropical cloud-topped boundary layers: 2. Cloud response to climate change. *J. Adv. Model. Earth Syst.*, *9*(1), 19–38. doi: 10.1002/2016MS000804

Taylor, K. E., Stouffer, R. J., & Meehl, G. A. (2012). An overview of CMIP5 and the experiment design. *Bull. Am. Meteorol. Soc.*, *93*, 485–498. doi: 10.1175/BAMS-D-11-00094.1

Vial, J., Bony, S., Dufresne, J.-L., & Roehrig, R. (2016). Coupling between lower-tropospheric convective mixing and low-level clouds: physical mechanisms and dependence on convection scheme. *J. Adv. Model. Earth Syst.*, *8*, 1892–1911. doi: 10.1002/2016MS000740

Vial, J., Bony, S., Stevens, B., & Vogel, R. (2017). Mechanisms and model diversity of trade-wind shallow cumulus cloud feedbacks: A review. *Surv. Geophys.*, *38*(6), 1331–1353. doi: 10.1007/s10712-017-9418-2

Vial, J., Dufresne, J.-L., & Bony, S. (2013). On the interpretation of inter-model spread in CMIP5 climate sensitivity estimates. *Climate Dynamics*, *41*(11), 3339–3362. doi: 10.1007/s00382-013-1725-9

Vogel, R., Albright, A. L., Vial, J., George, G., Stevens, B., & Bony, S. (2022). Strong cloud-circulation coupling explains weak trade cumulus feedback. *Nature*, *612*, 696–700. doi: 10.1038/s41586-022-05364-y

Vogel, R., Nuijens, L., & Stevens, B. (2016). The role of precipitation and spatial organization in the response of trade-wind clouds to warming. *J. Adv. Model. Earth Syst.*, *8*(2), 843–862. doi: 10.1002/2015MS000568

Zelinka, M. D., Myers, T. A., McCoy, D. T., Po-Chedley, S., Caldwell, P. M., Ceppi, P., ... Taylor, K. E. (2020). Causes of higher climate sensitivity in CMIP6 models. *Geophys. Res. Lett.*, *47*(1), e2019GL085782. doi: 10.1029/2019GL085782

Table 1. Absolute change between simulations, and relative change per change in SST from PD to EC, of the 24 h mean of cloud fraction (CF), liquid water path (LWP), and short-wave cloud radiative effect (SWCRE). The final row gives the change from simulation CTL to P2S of cumulus clouds under idealized climate change in the multimodel ensemble of Blossey et al. (2013).

	ΔCF	ΔLWP ($\mathrm{g\,m^{-2}}$)	ΔSWCRE ($\mathrm{W\,m^{-2}}$)	$\frac{\Delta \mathrm{CF}}{\mathrm{CF}\Delta \mathrm{SST}}$ ($\%\,\mathrm{K^{-1}}$)	$\frac{\Delta \mathrm{LWP}}{\mathrm{LWP}\Delta \mathrm{SST}}$ ($\%\,\mathrm{K^{-1}}$)	$\frac{\Delta \mathrm{SWCRE}}{\mathrm{SWCRE}\Delta \mathrm{SST}}$ ($\%\,\mathrm{K^{-1}}$)
$\mathcal{F}_{\mathrm{PD}} \rightarrow \mathcal{F}_{\mathrm{EC}}^{-}$	-0.002	-0.8	0.5			
$\mathcal{F}_{\mathrm{EC}}^{-} \rightarrow \mathcal{F}_{\mathrm{EC}}$	-0.004	-1.9	0.7			
$\mathcal{F}_{\mathrm{PD}} \rightarrow \mathcal{F}_{\mathrm{EC}}$	-0.007	-2.7	1.3	-4.3	-12.8	-4.7
$\mathcal{S}_{\mathrm{PD}} \rightarrow \mathcal{S}_{\mathrm{EC}}$	-0.004	-1.0	0.4	-2.7	-6.3	-2.2
$\mathcal{F}_{\mathrm{PD}}^{*} \rightarrow \mathcal{F}_{\mathrm{EC}}^{*}$	-0.009	-4.2	1.7	-5.4	-12.2	-6.1
$\mathcal{F}_{\mathrm{PD}}^{**} \rightarrow \mathcal{F}_{\mathrm{EC}}^{**}$	-0.011	-5.7	3.1	-6.2	-13.5	-9.9
CTL$\rightarrow$PS2	-0.011	0.6	1.1	-3.1	1.0	-2.5

Figure 1. Trade cumulus evolution in the simulations: (a) $\mathcal{F}_{\mathrm{PD}}$, (b) $\mathcal{F}_{\mathrm{EC}}^{-}$, (c) $\mathcal{F}_{\mathrm{EC}}$, (d) $\mathcal{S}_{\mathrm{PD}}$, and (e) $\mathcal{S}_{\mathrm{EC}}$. Sunrise (first column) is at 09h47m UTC (fractional day of year d = 32.41), sunset (last column) at 21h18m UTC (fractional day of year d = 32.89).

Figure 2. Time series from the simulation $\mathcal{F}_{\mathrm{PD}}$ (blue), $\mathcal{F}_{\mathrm{EC}}^{-}$ (cyan) and $\mathcal{F}_{\mathrm{EC}}$ (red), $\mathcal{S}_{\mathrm{PD}}$ (light green), and $\mathcal{S}_{\mathrm{EC}}$ (dark green) of (a) cloud fraction, (b) liquid water path, and (c) short-wave cloud radiative effect (shading indicates nighttime), and spectra at 18h00m UTC (d = 32.75) of (d) TKE production due to buoyancy in the cumulus layer, (e) variance of water vapor in the cumulus layer, and (f) variance of the short-wave cloud radiative effect.

Figure 3. Change from simulation $\mathcal{F}_{\mathrm{PD}}$ to $\mathcal{F}_{\mathrm{EC}}^{-}$ (a–d) and from $\mathcal{F}_{\mathrm{EC}}^{-}$ to $\mathcal{F}_{\mathrm{EC}}$ (e–h) in total water flux (a, e), liquid water (b, f), TKE production due to buoyancy (c, g), and radiative heating (d, h). The base of active cloud convection (dashed, SI) and the inversion (solid) from $\mathcal{F}_{\mathrm{EC}}^{-}$ (a–d) and $\mathcal{F}_{\mathrm{EC}}$ (e–h) are shown. An open triangle marks sunrise, a solid triangle sunset.

Figure 1.

09h47m UTC (d = 32.41)

16h00m UTC (d = 32.67)

18h00m UTC (d = 32.75)

21h18m UTC (d = 32.89)

a F_{PD}

b F^{-}_{EC}

c F_{EC}

d S_{PD}

e S_{EC}

km

0 50 100 150

0 50 100 150 km

0 0.1 0.5 1 2 4 6 8 10 12 15 20 25 30 40 50 60 80 100

Optical depth

Figure 2.

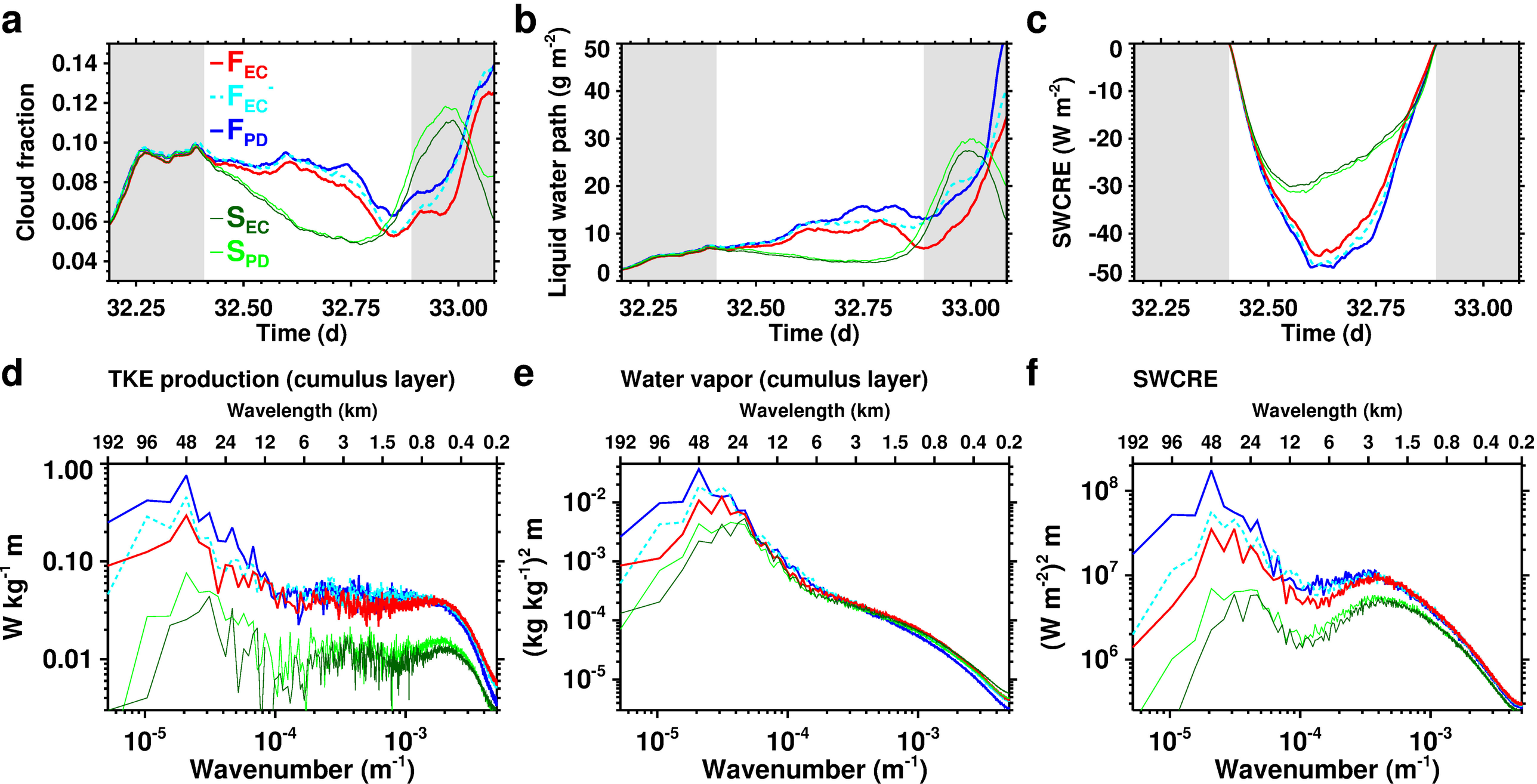
a
Cloud fraction
0.14
0.12
0.10
0.08
0.06
0.04
F_{EC}
F_{EC}^{-}
F_{PD}
S_{EC}
S_{PD}
32.25
32.50
32.75
33.00
Time (d)
b
Liquid water path (g m^{-2})
50
40
30
20
10
0
32.25
32.50
32.75
33.00
Time (d)
c
SWCRE (W m^{-2})
0
-10
-20
-30
-40
-50
32.25
32.50
32.75
33.00
Time (d)
d
TKE production (cumulus layer)
Wavelength (km)
192 96 48 24 12 6 3 1.5 0.8 0.4 0.2
W kg^{-1} m
1.00
0.10
0.01
10^{-5}
10^{-4}
10^{-3}
Wavenumber (m^{-1})
e
Water vapor (cumulus layer)
Wavelength (km)
192 96 48 24 12 6 3 1.5 0.8 0.4 0.2
(kg kg^{-1})^2 m
10^{-2}
10^{-3}
10^{-4}
10^{-5}
10^{-5}
10^{-4}
10^{-3}
Wavenumber (m^{-1})
f
SWCRE
Wavelength (km)
192 96 48 24 12 6 3 1.5 0.8 0.4 0.2
(W m^{-2})^2 m
10^{8}
10^{7}
10^{6}
10^{-5}
10^{-4}
10^{-3}
Wavenumber (m^{-1})

Figure 3.

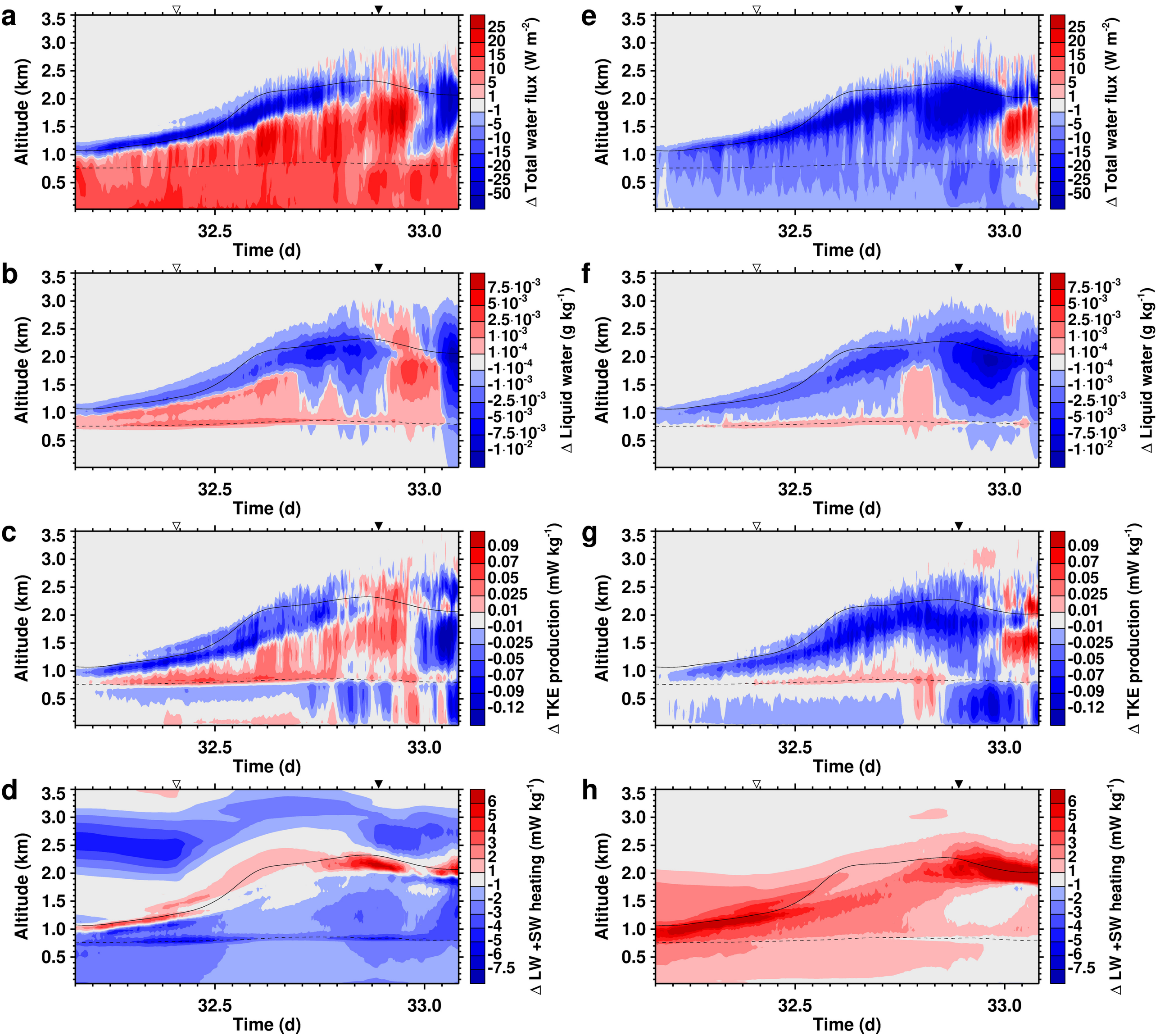
a
b
c
d
e
f
g
h
Altitude (km)
Time (d)
32.5
33.0
Δ Total water flux (W m-2)
Δ Liquid water (g kg-1)
Δ TKE production (mW kg-1)
Δ LW +SW heating (mW kg-1)